

A Journal of the Gesellschaft Deutscher Chemiker

Angewandte Chemie

GDCh

International Edition

www.angewandte.org

Accepted Article

Title: Tailoring Coordination Microenvironment of Nickel Molecular Complexes for Electrooxidation of Organic Nucleophiles

Authors: Chengdong Yang, Yun Gao, Wenwen Cai, Yueqing Wang, Jizhen Ma, and Jintao Zhang

This manuscript has been accepted after peer review and appears as an Accepted Article online prior to editing, proofing, and formal publication of the final Version of Record (VoR). The VoR will be published online in Early View as soon as possible and may be different to this Accepted Article as a result of editing. Readers should obtain the VoR from the journal website shown below when it is published to ensure accuracy of information. The authors are responsible for the content of this Accepted Article.

To be cited as: *Angew. Chem. Int. Ed.* **2025**, e202509377

Link to VoR: <https://doi.org/10.1002/anie.202509377>

RESEARCH ARTICLE

Tailoring Coordination Microenvironment of Nickel Molecular Complexes for Electrooxidation of Organic Nucleophiles

Chengdong Yang^a, Yun Gao^b, Yueqing Wang^a, Wenwen Cai^a, Jizhen Ma^a, and Jintao Zhang^{a*}

[a] Dr. C.D. Yang, Dr. Y.Q. Wang, W.W. Cai, J.Z. Ma, Prof. J.T. Zhang

Key Laboratory for Colloid and Interface Chemistry, Ministry of Education School of Chemistry and Chemical Engineering, Shandong University, Jinan 250100, China

E-mail: jtzhang@sdu.edu.cn (J.T. Zhang)

[b] Y. Gao

Engineering Research Center of Advanced Rare Earth Materials, Department of Chemistry, Tsinghua University, Beijing 100084, China

Supporting information for this article is given via a link at the end of the document.

Abstract: Electrochemical oxidation of organic nucleophiles to value-added chemicals using nickel-based catalysts is promising yet hindered by the dynamic evolution of nickel coordination structures during catalysis. Herein, we engineered atomically exposed nickel molecular catalysts anchored on functional carbon black through tailored aromatic ligands coordination. This unique spatial coordination structure efficiently promotes the reconstruction of high-valence Ni^{III}-OOH sites, which boost electrooxidation of 18 organic substrates with peak current density exceeding 800 mA cm⁻². Especially, the optimal electrocatalyst achieves record mass activities of 4.38 and 4.26 A mg_{Ni}⁻¹ for methanol and ethylene glycol oxidation, respectively. In-situ characterization and theoretical analyses elucidate that the atomically exposed Ni^{III}-OOH centers would directly adsorb organic substrates, thereby enhancing C-C/C-H bonds cleavage efficiency. Meanwhile, the proton abstraction from C-H bond would enable reversible redox cycling between Ni^{II}-OH and Ni^{III}-OOH, sustaining catalytic activity. This study advances the understanding of organic oxidation mechanisms and showcases the great potential of molecular complexes in electrocatalysis.

Introduction

Replacing the sluggish oxygen evolution reaction (OER) by electrooxidation of organic substrates have demonstrated with low energy consumption for hydrogen (H₂) productions at cathode and value-added chemicals and fuel generations at anode^[1]. In particular, this technology with mild operation conditions shows significant promise in various fields, such as biomass update^[2], raw materials processing^[3], waster plastic cycle^[4], and wastewater pollution treatments^[5] (**Figure 1a**). Recently, nickel-based catalysts are particularly advantageous for catalyzing organic electrooxidation^[6], exhibiting much lower onset potential than OER^[7]. The in-situ generation of nickel oxide hydroxide (NiOOH) species with highly electrophilic lattice oxygen atoms endows their efficiently electrochemical activity^{[8],[9]}. However, the immovable lattice oxygen species in bulk NiOOH would shield the directly adsorption of reactants on Ni sites^[10] (**Figure 1b**), thus leading to low accessibility of nickel sites and limited diffusion rates of reactant. These drawbacks account for slow organics oxidation reaction kinetics, limiting current density to below 500 mA cm⁻²^[11]. Furthermore, for electrooxidation of polyhydric alcohols, the sluggish cleavage of C-C bonds leads to unsatisfied reaction activities and product selectivity^[12]. Although the oxygen vacancy-mediated strategies have been proposed^[13], the limited availability of oxygen vacancies depress the catalytic efficiency,

and the mechanisms behind C-C bonds cleavage are still not fully understood. Therefore, it is still challenging to properly adjust the structure and surface properties of Ni-based catalysts to fully expose metal sites for advancing organics oxidation processes.

In metalloprotein enzymes, organic ligands coordinating with metallic sites have demonstrated the ability to fine-tune catalytic environments, significantly impacting enzyme catalytic efficiency^[14]. The artificial organic-metal hybrids, such as metal-organic frameworks (MOFs) and coordination polymers featured with the flexible coordination environments^[15], have also exhibited unexpected catalytic activities and selectivity in various fields^[16], providing great potential to overcome the innate limitation of traditional catalysts. However, the organic electrooxidation is mainly proceeded on the near-surface regions of a catalyst, thereby the bulk organic-metal hybrids with poor conductivity and complicated structural reconstructions would disturb the essential understanding of structure-activity relationships^[17]. Additionally, the low accessibility of inner catalytic sites limit catalytic efficiency, and the occupied metal orbitals fail to directly activate the C-C bonds^[18]. Therefore, at the atomic scale, creating molecularly dispersed organic-metal hybrid catalysts with coordinatively unsaturated states is essential for uncovering the reaction mechanisms of organic oxidation process.

Herein, we developed a series of nickel-based isostructural molecular complexes through coordinating nickel ions with aromatic carboxylate ligands on conductive carbon substrates. The π - π stacking interactions between aromatic ligands and the carbon support efficiently stabilize the highly accessible nickel sites. Especially, the geometric diversity of ligands provides high flexibility in regulating the coordination environments and electron structures of nickel sites supported, which is key for the dynamic generation of highly accessible Ni^{III}-OOH sites via sequential OH⁻ nucleophilic attack and dehydrogenation. These hypervalent Ni^{III}-OOH sites with electrophilic oxygen enable superior electrocatalytic oxidation of 18 organic molecules with high-current density over 800 mA cm⁻². In particular, methanol and ethylene glycol (EG) oxidation achieved high mass activities of 4.38 and 4.26 A mg_{Ni}⁻¹ at 1.45 V, respectively. *In situ* characteristics and theoretical analysis confirm that the atomically exposed nickel sites would benefit C-H and C-C bond cleavage via unoccupied nickel *d* orbitals (**Figure 1c**), aided by OH⁻ nucleophilic attack. Simultaneously, the electrophilic oxygen species in Ni^{III}-OOH facilitate proton abstraction from C-H bonds, stabilizing the coordination structures of Ni-based molecular complexes due to the reversible Ni^{II}-OH/Ni^{III}-OOH redox cycle.

RESEARCH ARTICLE

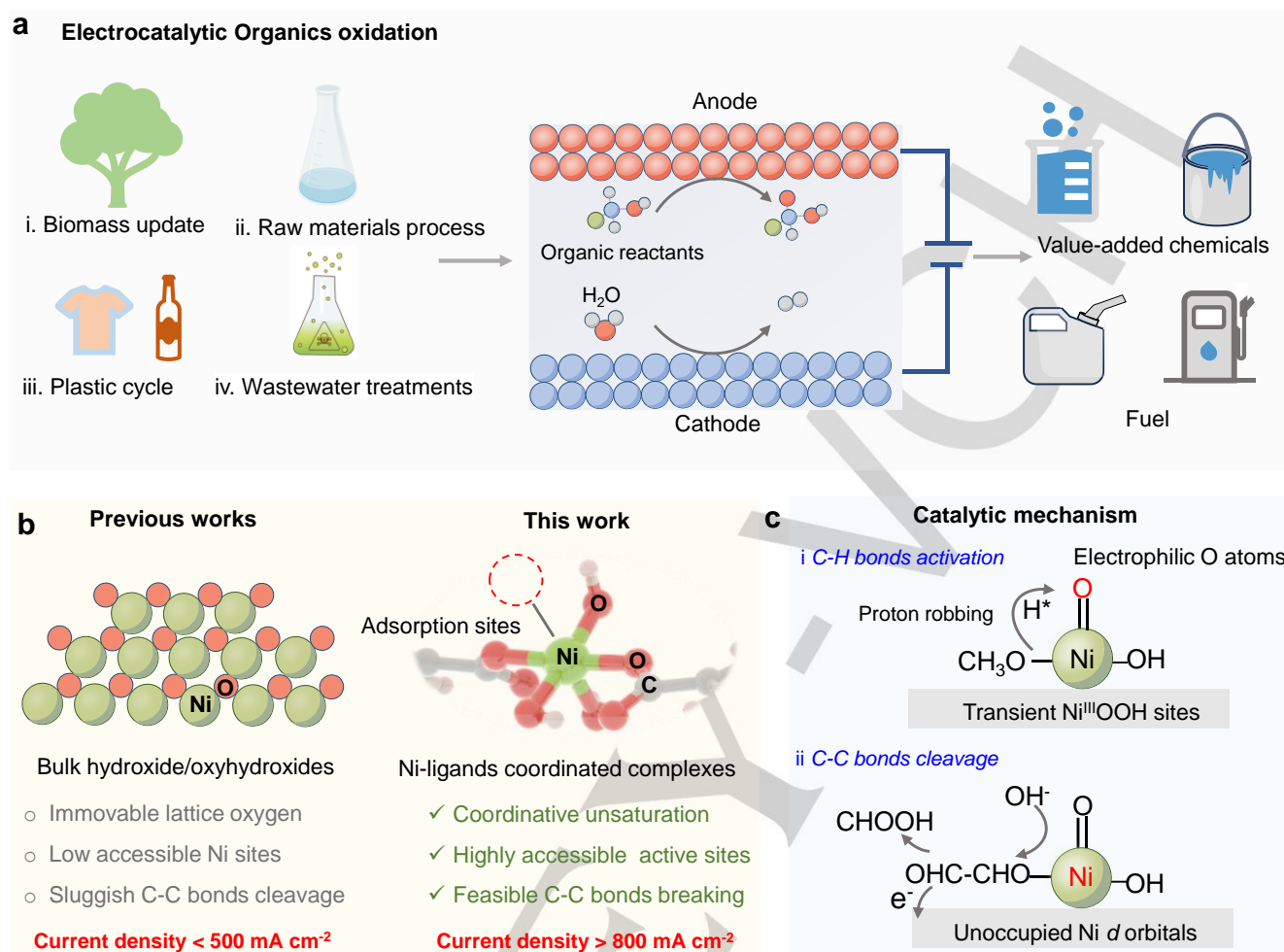


Figure. 1 a) Schematic illustration of the electrolysis system coupling hydrogen-evolution reaction with organics oxidation. b) Overview of various anode catalysts for organics electrooxidation. c) Diagram depicting the cleavage of C-H and C-C bonds on nickel-based molecular complexes, primarily driven by electrophilic oxygen species and coordinatively unsaturated nickel sites, respectively.

This work would provide a foundational understanding of electrocatalytic oxidation mechanisms and highlight the potential of molecular complexes for advanced catalytic applications.

Results and Discussion

A series of isostructural Ni-based molecular complexes were synthesized by assembling of Ni²⁺ ions with various aromatic organic linkers on oxidized Ketjenblack (OKB) (Figure 2a), referred to as Ni-PTA/OKB, Ni-BPDA/OKB, and Ni-PTDA/OKB, respectively. Importantly, the different geometry configurations and molecular structures of these aromatic ligands allow rational manipulation of the π - π stacking interactions between the molecular complexes and OKB supports^[19]. The oxygen functional groups on carbon support would also facilitate the anchoring of nickel-ligand coordination sites through strong π - π stacking interactions. Transmission electron microscopy (TEM) images reveal that the OKB supports are coralloid nanostructure with an average branch size of 30–40 nm (Figure S1). The absence of MOFs sheets in these Ni-based molecular complexes suggests that the nickel sites are molecularly dispersed on the carbon supports (Figure 2b and Figure S2-S3). For comparison, the direct assembling Ni²⁺ ion with aromatic ligands in the absence of OKB support leads to the formation of nickel-based

MOFs layers (Ni-MOL) with 2D nanosheets structure (Figure S4). X-ray diffraction patterns of these Ni-based molecular complexes only display the characteristic diffraction peaks of carbon substrate (Figure S5-S6), confirming the molecular dispersion of nickel sites. Furthermore, high-resolution high-angle annular dark-field scanning TEM (HAADF-STEM) of Ni-BPDA/OKB exhibits isolated bright dots (marked by yellow circles) on carbon support, unveiling the atomic dispersion of nickel centers (Figure 2c and Figure S7). STEM elemental mapping and line scanning results demonstrate the uniform distribution of Ni elements on carbon supports (Figure S8-S9). Then, Fourier transform infrared (FTIR) spectra show noticeable redshifts of the $\nu(\text{C}=\text{O})$ peak to 1600 cm⁻¹ and the $\nu(\text{C}-\text{O})$ peak to 1385 cm⁻¹ in these molecular complexes, compared with the organic ligands, attributed to the coordination between nickel ion and carboxylic acid group (Figure S10).

X-ray photoelectron spectroscopy (XPS) analysis revealed that the Ni loading in Ni-BPDA/OKB was approximately 6.72 wt% (Table S1). And high-resolution XPS spectra demonstrated a shift in the Ni 2p peaks of Ni-BPDA/OKB to higher binding energies compared to Ni-BPDA-MOL, thus demonstrating electron transfer between Ni sites and carbon support (Figure 2d and Figure S11). This shift can be attributed to strong π - π stacking interactions^[20],

RESEARCH ARTICLE

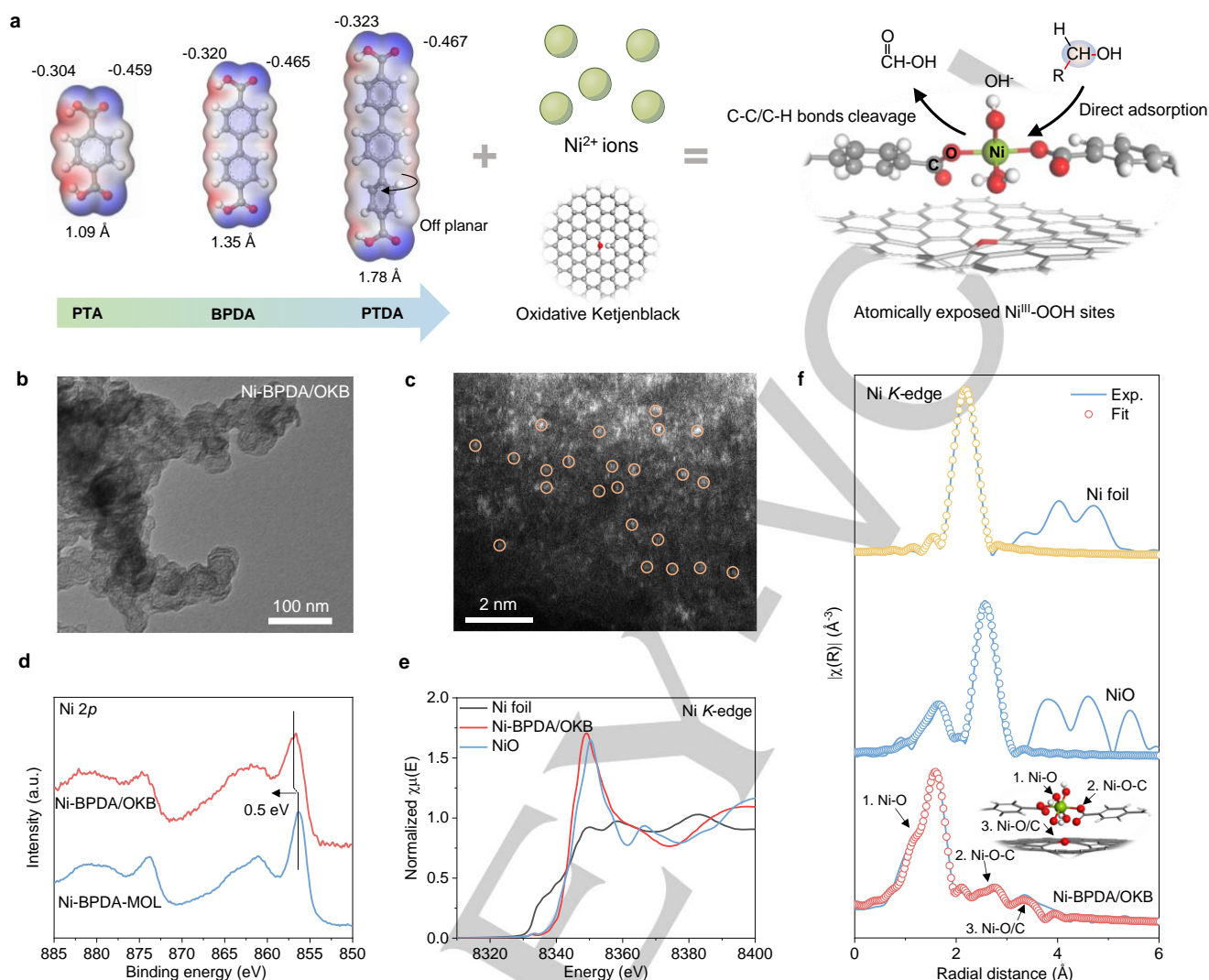


Figure 2. The structural characterization of Ni-based molecular complexes. a) Schematic representation of the molecular complexes assembly process. b) TEM image and c) High-resolution HAADF-STEM image of Ni-BPDA/OKB. d) High-resolution XPS spectra of Ni 2p in Ni-BPDA/OKB and Ni-BPDA-MOL. e) Normalized XANES spectra at the Ni K-edge of Ni-BPDA/OKB. f) EXAFS spectra in R-space with corresponding fitting curves for NiO, Ni-BPDA/OKB, and Ni foil.

leading to higher valence state of Ni sites in Ni-BPDA/OKB. The Ni-BPDA/OKB exhibits a more obvious metal-hydroxides peak in O 1s spectra compared to Ni-BPDA-MOL (Figure S12), indicating that the atomically exposed Ni sites tend to be attacked by the H₂O in air atmosphere. Additionally, the X-ray absorption near-edge structure (XANES) spectra at the Ni K-edge exhibit a slightly higher absorption position than that of NiO, suggesting an average valence state higher than Ni²⁺ (Figure 2e). Fourier transforms (FT) and wavelet-transforms (WT) analyses of the extended X-ray absorption fine structure (EXAFS) spectra at the Ni K-edge exhibit a primary peak at ~1.97 Å and a weaker peak at ~2.45 Å (Figure S13-16). These peaks correspond to Ni-O bonds in first coordination shell and Ni-O-C bonds in second coordination shell, respectively (Figure 2f and Table S2). Notably, the Ni-O-C bonds, with coordination numbers around 1.9, indicates that the unsaturated Ni sites are coordinated with two BPDA ligands. The presence of long-range Ni-C/O bonds confirms the interactions between Ni sites and OKB supports, which would stabilize the structure of molecular complexes. Besides, no Ni-Ni or Ni-O-Ni bond in EXAFS spectrum can be detected, confirming the atomical dispersion of nickel sites in Ni-BPDA/OKB.

Electrocatalytic performance

Cyclic voltammetry (CV) curves were conducted to investigate the Ni^{II} to Ni^{III} oxidation (Figure 3a). The Ni-BPDA/OKB exhibit a pronounced quasi-reversible redox peak at 1.26 V compared to Ni-PTDA/OKB at 1.27 V and Ni-PTA/OKB at 1.30 V, indicating an easier redox process for Ni^{II}/Ni^{III} in Ni-BPDA/OKB^[21]. This can be contributed to fast electron transferring between molecular complexes and OKB substrate through the strong π - π stacking interactions^[20c]. Then, the electrocatalytic oxidation activities of 18 organic substrates, including primary alcohols, aldehydes, amines, and compounds with multiple reactive groups were evaluated using linear sweep voltammetry (LSV) curves in 1.0 M KOH (Figure 3b). The Ni-BPDA/OKB shows low onset potential and rapidly-growing current density for various organic substrates, demonstrating the exceptional electrocatalytic activities (Figure S17-25). Importantly, the Ni-BPDA/OKB exhibits an ultra-high mass activity of 4.38 A mg_{Ni}⁻¹ at 1.45 V for methanol oxidation, confirming the outstanding intrinsic organic oxidation activities for organic compounds.

RESEARCH ARTICLE

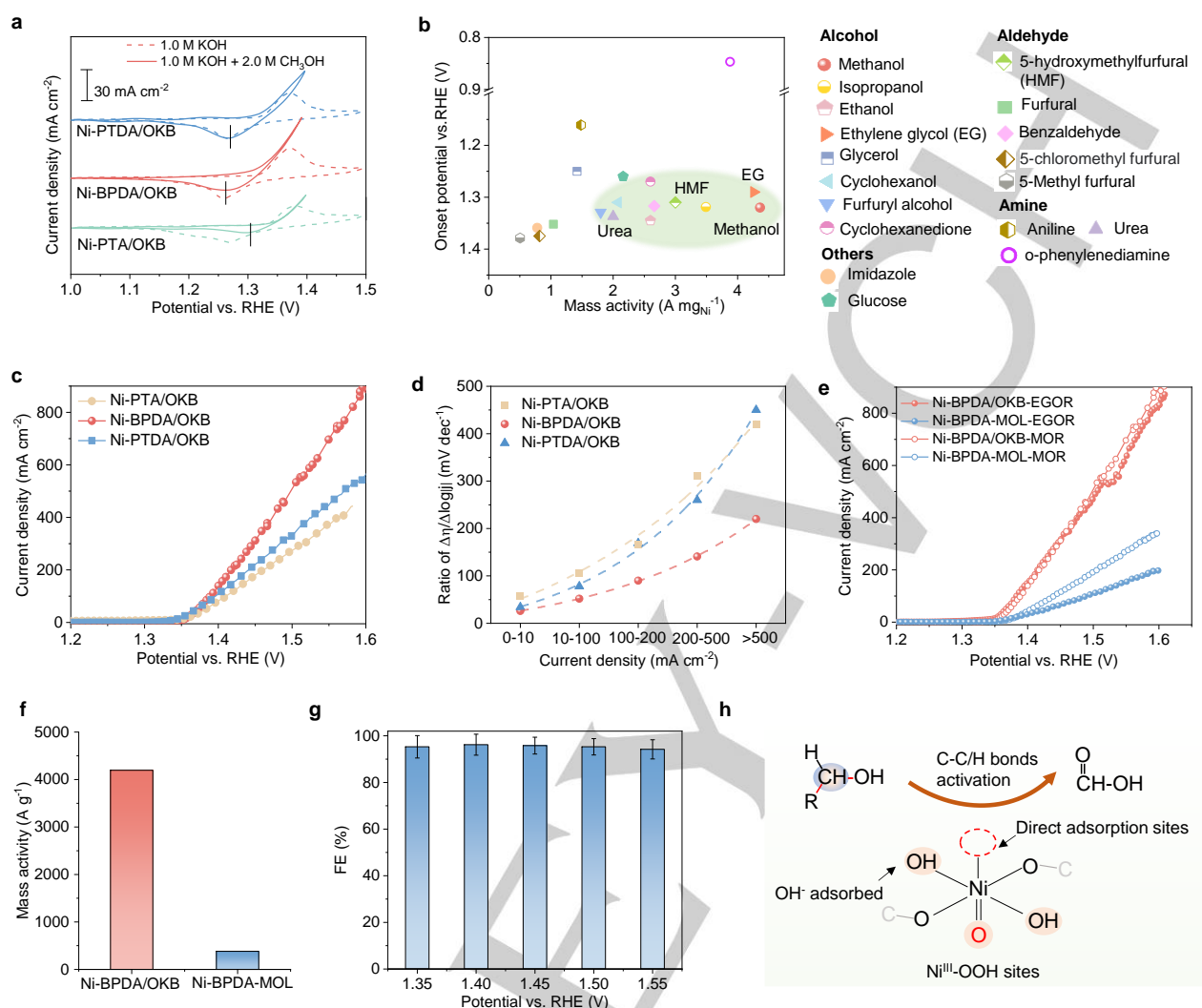


Figure 3. Analysis of catalytic performances. **a** The CV curves of different catalysts with or without 2.0 M methanol. **b** Onset potential and mass activity of Ni-BPDA/OKB for 18 different substrates. **c** Methanol oxidation polarization curves of different catalysts with 2.0 M methanol. **d** Ratios of $\Delta\eta/\Delta\log|j|$ for the different catalysts in different current density ranges. **e** EG oxidation polarization curves of Ni-BPDA/OKB and Ni-BPDA-MOL with 0.6 M EG. **f** Mass activity obtained from EG oxidation polarization curves of Ni-BPDA/OKB and Ni-BPDA-MOL. **g** Faradaic efficiency for formate production from EG oxidation on the Ni-BPDA/OKB. **h** Schematic diagram of possible activation of C-H and C-C bonds on coordinatively unsaturated Ni sites in Ni-BPDA/OKB during electrocatalysis.

Methanol oxidation reaction (MOR) is employed to evaluate C-H bond cleavage kinetics in 1.0 M KOH (Figure S26-S27). The Ni-based molecular complexes show faster reaction kinetics than that of corresponding bulk Ni-MOL, indicating the superior catalytic performance due to the highly accessible nickel sites (Figure S28). Besides, the Ni-BPDA/OKB only requires 1.47 V to reach a current density of 400 mA cm⁻², significantly lower than those of Ni-PTDA/OKB (1.52 V) and Ni-PTA/OKB (1.55 V) (Figure 3c). The ratios of overpotential ($\Delta\eta$) to current density ($\Delta\log|j|$) for Ni-BPDA/OKB is lowest (<200 mV dec⁻¹), indicating the fastest reaction kinetics (Figure 3d and Figure S29)^[22]. The outstanding catalytic performance of Ni-BPDA/OKB can be attributed to rapid electron transfer between the molecular complexes and carbon substrates. Ion chromatography (IC) and ¹H nuclear magnetic resonance (NMR) spectroscopy analyses revealed the high Faradaic efficiencies (FE) of formate production, exceeding 94% under various applied potentials (Figure S30-S31). Besides, the potential-dependent Nyquist and Bode plots obtained from *in situ* electrochemical impedance spectroscopy confirmed the fast electron transfer (Figure S32). The long-term durability test

performed at 1.4 V and 1.5 V (without iR compensation) demonstrate the stability of Ni-organic coordination structures during electrooxidation (Figure S33).

Ethylene glycol oxidation reaction (EGOR) studies showed similar catalytic behaviors as MOR, with Ni-BPDA/OKB exhibiting high catalytic efficiency for C-C bond cleavage (Figure 3e). The Ni-BPDA/OKB achieve an ultra-high current density of 800 mA cm⁻² at 1.59 V, outperforming previously reported EGOR catalysts with current density below 500 mA cm⁻² (Figure S34 and Table S3). In contrast, the Ni-BPDA-MOL shows much slower EGOR catalytic kinetic than that of MOR. This slower rate is attributed to the sluggish C-C bond breaking on saturated Ni-BPDA-MOL with fewer accessible nickel sites. However, the Ni-BPDA/OKB shows an ultra-high EGOR mass activity of 4.26 A mgNi⁻¹ at 1.45 V, which is 13 times higher than that of Ni-BPDA-MOL (Figure 3f). IC and ¹H NMR spectra confirmed the high FE of formate production across a wide range of potentials (Figure 3g and Figure S35-S36), resulting from the effective cleavage of C-C bonds. The outstanding electrooxidation performance would be attributed to the coordinatively unsaturated environments in Ni-BPDA/OKB

RESEARCH ARTICLE

that promote the direct EG adsorption on atomically exposed Ni sites, thus facilitating C–C bonds cleavage via the unoccupied nickel *d* orbitals^[23] (Figure 3h). This structural advantage highlights the significance of atomically dispersed nickel sites in enhancing catalytic activity for organic oxidations.

The dynamical structural evolution and reaction pathways on Ni-BPDA/OKB were further elucidated using *in situ* Raman measurements in different electrolytes (Figure S37–S38). Under OER conditions, new Raman bands appear at 471 and 552 cm^{−1} with a potential of 1.30 V (Figure 4a), assigning to the bending and stretching vibrations of Ni³⁺–O structures in γ-Ni^{III}-OOH^[24], respectively. These characteristic bands of Ni^{III}-O remained stable after reactions (Figure S39), indicating that the Ni^{III}-OOH structure once formed, is irreversible during OER. In comparison, during MOR, the bending and stretching vibration peaks show a blue shift to 476 and 560 cm^{−1}, respectively, suggesting the weakened Ni^{III}-O bond in Ni^{III}-OOH (Figure 4b). Interestingly, upon removal of the voltage input, the Ni^{III}-OOH species gradually disappeared after 60 s, thus demonstrating the transient nature of these active sites (Figure 4c and Figure S40). The transient Ni^{III}-OOH with highly electrophilic oxygen species, facilitates proton abstraction from α-C–H bonds, thereby achieving a reversible redox process between Ni^{II}-OH and Ni^{III}-OOH and the regeneration of coordination structures in Ni-BPDA/OKB. *In situ* Raman spectra also reveal that the Ni^{III}-OOH formation is driven by the dehydrogenation of OH* adsorbed on highly oxidative nickel atoms (Figure 4d).

To further explore the dynamic reconstruction of Ni^{III}-OOH, CV curves were conducted with varying organic substrate concentrations. At high substrate concentrations, the CV curves of MOR and EGOR exhibit high current density during the

negative scan, thus indicating a hysteresis effect (Figure 4e and Figure S41). The hysteresis can be interpreted by the insufficient Ni^{III}-OOH active sites during the initial positive scan, demonstrating that the favorable adsorption of organic substrates would compete with the formation of active Ni^{III}-OOH. This standpoint can also be confirmed by the delayed MOR onset potential and the weakening of Ni^{II} → Ni^{III} redox peaks at higher methanol concentrations (Figure S42–S43). Furthermore, the pristine Ni-BPDA/OKB presents increasing current density over time, demonstrating a self-activation process wherein Ni sites undergo gradual structural reconstruction to form Ni^{III}-OOH species (Figure S44). Compared with Ni-BPDA/OKB, the Ni-BPDA/OKB-OOH obtained by direct activation in 1.0 M KOH, exhibits a lower MOR onset potential but suboptimal catalytic performance at high-current densities (Figure S45), likely due to disrupted coordination structures. The above findings demonstrate that the Ni^{III}-OOH species, featuring highly electrophilic oxygen atoms and atomically exposed nickel sites, play a pivotal role in driving the oxidation of organic substrates. Meanwhile, intensive proton transfer from activated C–H bonds ensure structural stability by reduction of the active centers.

Then *in-situ* X-ray absorption spectroscopy (XAS) analysis under MOR conditions has been conducted. As shown in Figure 5a, b, the Ni K-edge gradually shifts to higher energy as the applied potential increases from open circuit potential (OCP) to 1.5 V, indicating an increase in the oxidation state of Ni species. This high valence state is attributed to the dynamic structure evolution of Ni-ligand coordination structure in alkaline conditions. The spent Ni-BPDA/OKB catalyst after MOR shows a lower Ni valence state compared to that after OER, thus indicating the presence of a reversible Ni^{III}-OOH center during MOR.

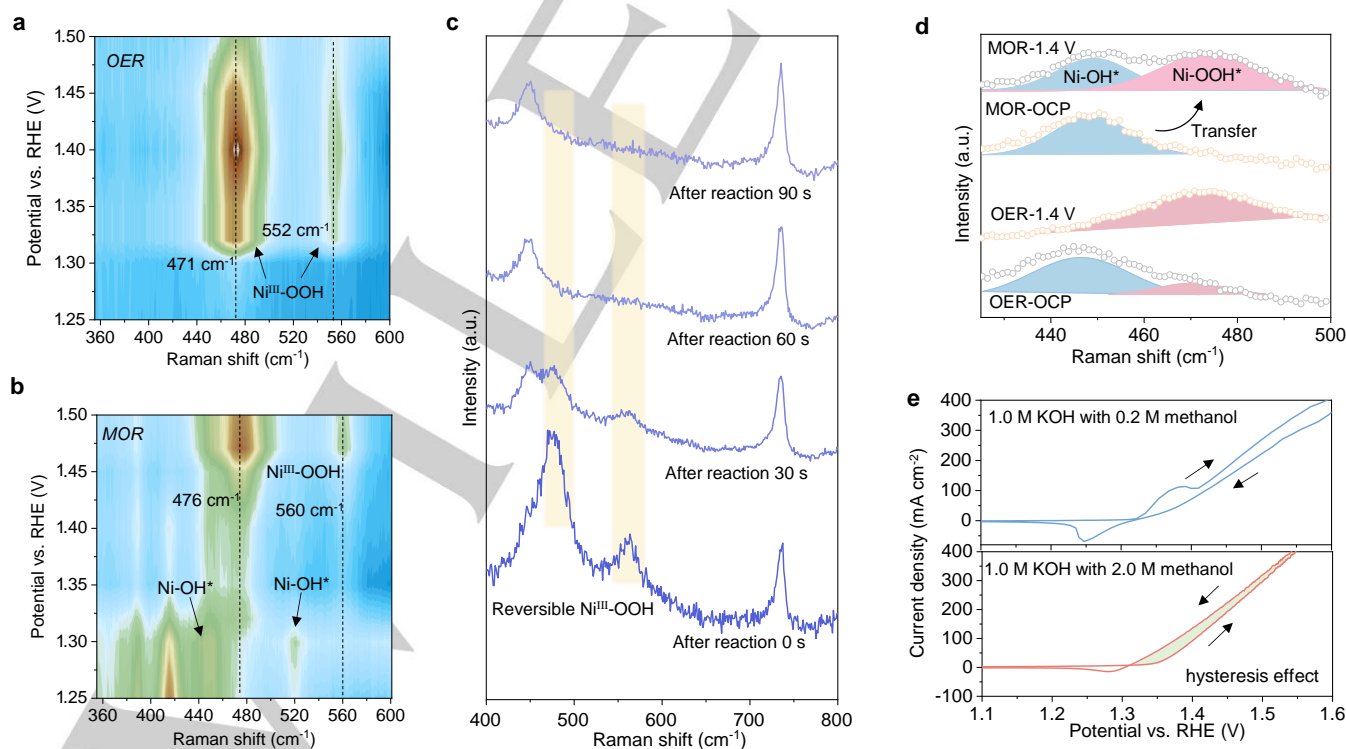


Figure 4. Study of structure evolution of transient Ni^{III}-OOH active center. In situ Raman spectra of Ni-BPDA/OKB for a) OER and b) MOR. c) In situ Raman spectra of Ni-BPDA/OKB after reaction. d) Deconvolution of bending vibration peaks of Ni^{III}-OOH for OER and MOR process. e) CV curves for MOR with 0.2 M and 2.0 M methanol concentrations.

RESEARCH ARTICLE

Furthermore, FT and WT analyses of EXAFS spectra for Ni-BPDA/OKB exhibit prominent Ni-O-Ni bonds at applied potentials of 1.40 and 1.50 V (Figure 5c, Figure S46-48), suggesting the formation of $\text{Ni}^{\text{III}}\text{-OOH}$ during electrooxidation process. The Ni-BPDA/OKB after MOR only exhibits a Ni-O bond at 2.07 Å, similar with that in pristine Ni-BPDA/OKB, indicating a reversible redox cycle between $\text{Ni}^{\text{III}}\text{-OOH}$ and center $\text{Ni}^{\text{II}}\text{-OH}$. Conversely, the Ni-BPDA/OKB after OER shows a prominent Ni-O bond at 2.05 Å and a weak Ni-O-Ni bond at 3.17 Å (Tables S4-S8), suggesting the formation of irreversible $\text{Ni}^{\text{III}}\text{-OOH}$ centers under these conditions. For Ni 2p XPS spectra, the Ni-BPDA/OKB exhibits a slight increase in the valence states of Ni after MOR (Figure 5d), which is consistent with XAS analysis. Furthermore, the HAADF-STEM image of Ni-BPDA/OKB after prolonged MOR show isolated bright dots (marked by yellow circle) (Figure 5e), demonstrating the stable nickel-ligand coordination structures.

Mechanism investigation

To further understand the pathways of organic oxidation on electrophilic transient $\text{Ni}^{\text{III}}\text{-OOH}$ sites, the attenuated total reflection surface-enhanced infrared adsorption spectroscopy (ATR-SEIRAS) was conducted (Figure S49). Before MOR, the $\nu(\text{C-OH})$ peak at 1228 cm^{-1} (Figure 6a and Figure S50) indicates the favorable adsorption of methanol on coordinatively unsaturated nickel sites. This is primarily due to the feasible electron donation from the σ -orbital of -OH group into the vacant d orbital of Ni^{2+} centers. As the potential increases above 1.35 V, this peak weakens, suggesting the consumption of methanol adsorbed. Besides, the emergence of a new $\nu(\text{C=O})$ peak at 1580 cm^{-1} confirms the formation of CHOO^{\cdot} .

Density functional theory calculations further elucidate the reaction pathways, using a model with nickel sites coordinated to

two ligands (Figure S51-S52). The Ni-BPDA/OKB exhibits the highest π - π stacking energy between Ni-molecular complexes and carbon substrate (Figure 6b), which would facilitate electron transfer. The π - π stacking interactions are influenced by both the length of aromatic nucleus and the geometry of organic ligands. The BPDA ligand, with longer benzene ring, leads to stronger π - π stacking interactions in Ni-BPDA/OKB compared to Ni-PTA/OKB. In contrast, the Ni-PTDA/OKB with longest benzene ring exhibits lower π - π stacking due to the reduced overlap of π -electron clouds caused by the off-plane conformations of PTDA ligands (Figure S53). This is further supported by Mulliken atomic charge analysis, which shows the highest valence state of Ni sites in Ni-BPDA/OKB (Figure S54-S55). An exponent relationship is observed between $\text{Ni}^{\text{II}}\text{-OH}$ dehydrogenation energy and π - π stacking energy for Ni-based molecular complexes (Figure 6c and Figure S56). This result unveils that the strong π - π stacking interactions would promote the dehydrogenation of $\text{Ni}^{\text{II}}\text{-OH}$ structure, thus facilitating the reconstruction of hypervalent $\text{Ni}^{\text{III}}\text{-OOH}$.

The reaction pathways for electrocatalytic MOR were investigated, starting with methanol adsorbed on $\text{Ni}^{\text{II}}\text{-OH}$ sites, followed by a stepwise dehydrogenation process. Optimized adsorption configurations and corresponding Gibbs energy diagrams reveal that the spontaneous dehydrogenation of O-H bonds in methanol can be driven by the highly oxidative $\text{Ni}^{\text{III}}\text{-OOH}$ species (Figure 6d and Figure S57). Proton abstraction from C-H bonds can be significantly facilitated by the electrophilic oxygen atoms in $\text{Ni}^{\text{III}}\text{-OOH}$ compared to $\text{Ni}^{\text{II}}\text{-OH}$ (Figure 6e and Figure S58). Importantly, this proton abstraction process not only benefits the activation and dehydrogenation of C-H bonds, but also aids in the reduction of $\text{Ni}^{\text{III}}\text{-OOH}$ to $\text{Ni}^{\text{II}}\text{-OH}$. Additionally, CHO^{\cdot} intermediates, formed from the dehydrogenation of $\text{CH}_2\text{O}^{\cdot}$,

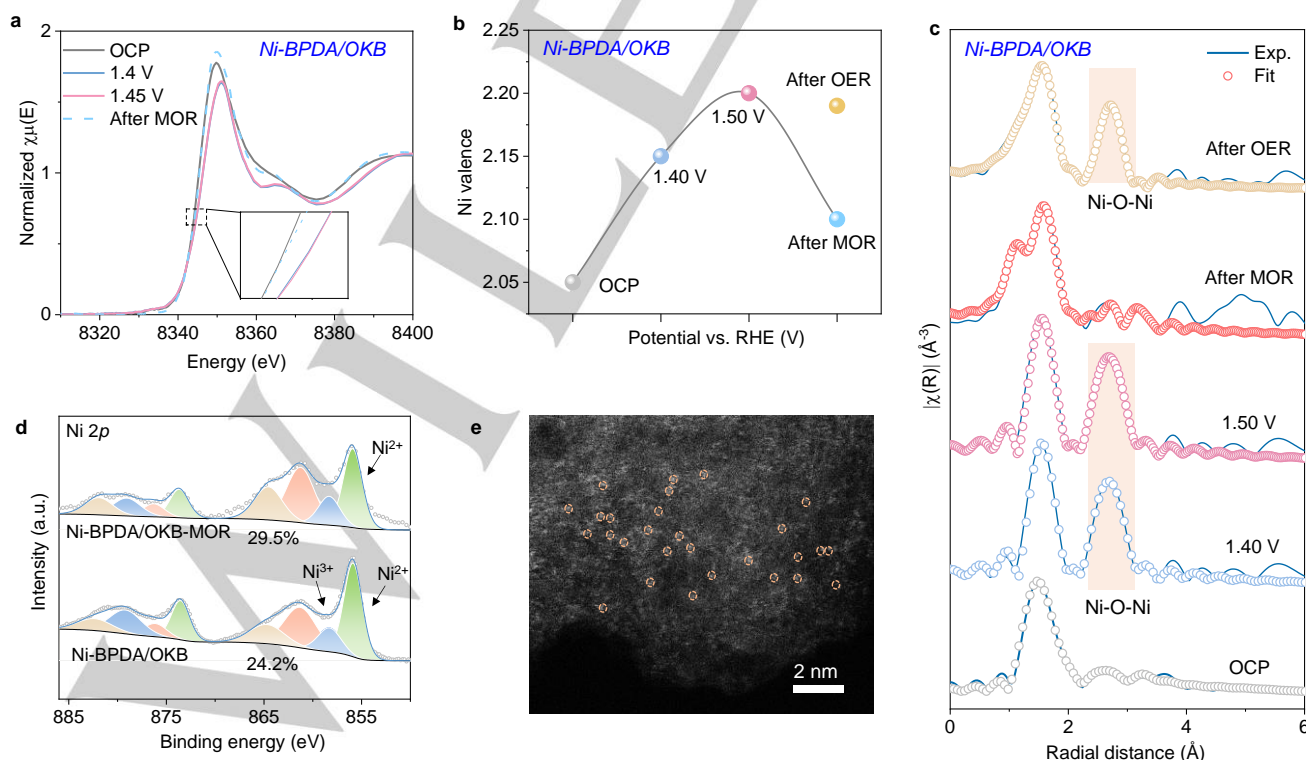


Figure 5. Structural characterizations of Ni-BPDA/OKB after electrocatalysis. a) in situ XANES spectra at the Ni K-edge for Ni-BPDA/OKB. b) Valence analysis of Ni-BPDA/OKB at different operation conditions. c) EXAFS in R-space with corresponding fitting curves for Ni-BPDA/OKB at different operation conditions. d) XPS spectra of Ni-BPDA/OKB and Ni-BPDA/OKB-MOR taken at Ni 2p. e) High-resolution HAADF-STEM image of Ni-BPDA/OKB after MOR.

RESEARCH ARTICLE

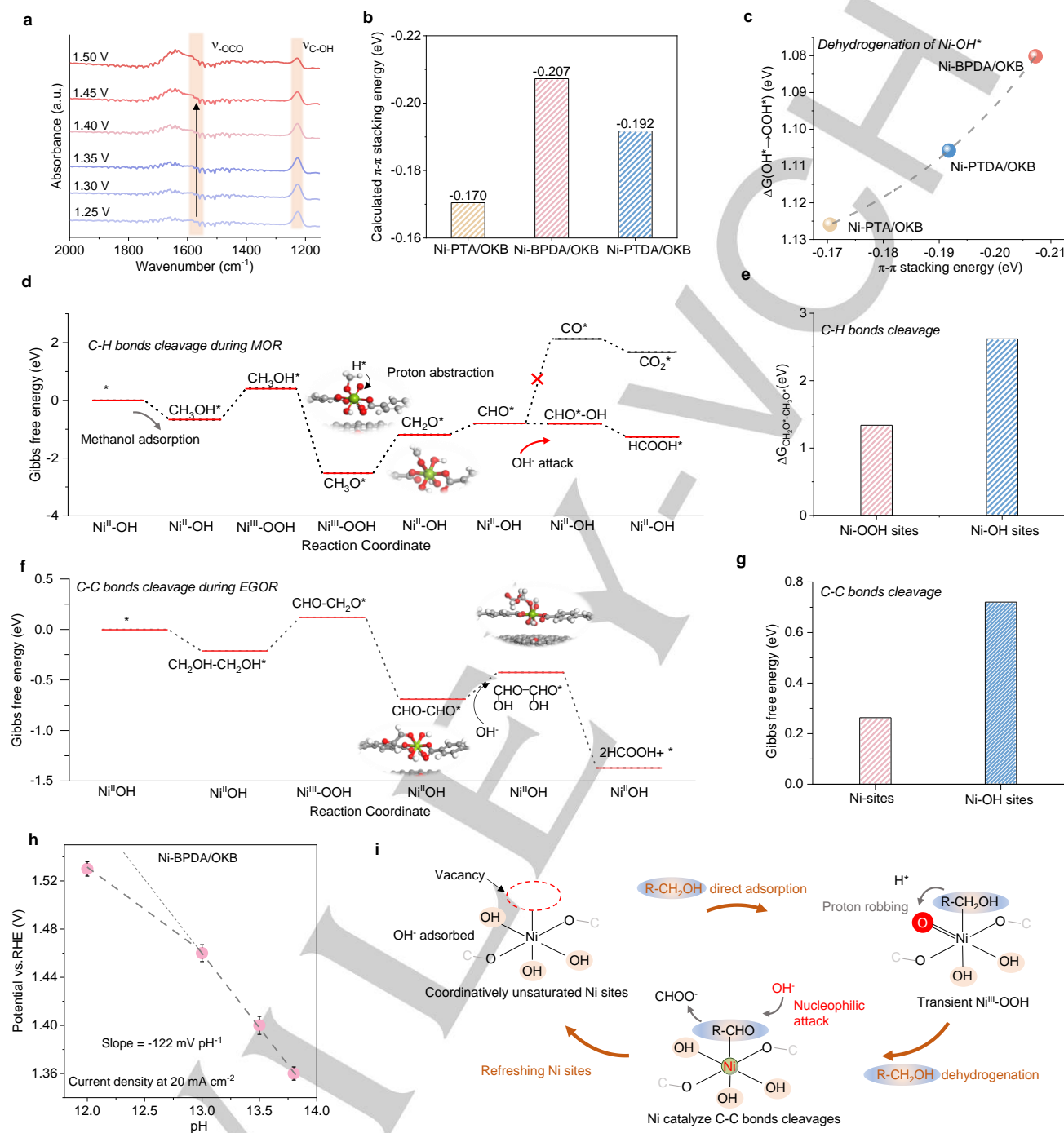


Figure 6. Understanding of the C-H/C-C bonds cleavage. a) *In situ* ATR-SEIRAS spectra of Ni-BPDA/OKB under different potentials. b) π - π stacking energy of different catalysts. c) Linear relationship between $\Delta G_{\text{O}^*-\text{H}} - \Delta G_{\text{OH}^*}$ and π - π stacking energy. d) Gibbs free energy diagrams for MOR using Ni-BPDA/OKB. e) Comparison of free energy diagrams for C-H bond dehydrogenation on $\text{Ni}^{\text{II}}\text{-OH}$ and $\text{Ni}^{\text{III}}\text{-OOH}$. f) Gibbs free energy diagrams for EGOR on Ni-BPDA/OKB. g) Gibbs free energy of C-C bond cleavage on Ni sites and oxygen atoms in $\text{Ni}^{\text{III}}\text{-OOH}$ species. h) Pourbaix diagram for EGOR under different pH conditions for Ni-BPDA/OKB. i) Schematic illustration of alcohol electrooxidation pathways on transient $\text{Ni}^{\text{III}}\text{-OOH}$.

are prone to be attacked by OH^- in electrolyte, thus leading to the spontaneous formation of formate (Figure S59). The Gibbs energy diagram unveils that the electrocatalytic conversion of CHO^* to CO^* is thermodynamically unfavorable ($\Delta G = 2.9 \text{ eV}$), confirming the selective production of formate over CO_2 .

The EGOR process was also calculated to analyze the kinetics of C-C bonds cleavage. Coordinatively unsaturated

nickel sites would facilitate the direct adsorption of EG, and continuous dehydrogenation results in the formation of CHO-CHO^* intermediate on nickel sites (Figure 6f and Figure S60). The CHO-CHO^* intermediate undergo C-C bond cleavage on nickel sites, assisted by the OH^- nucleophilic attack, thus leading to the rapid formate production. However, the CHO-CHO^* adsorbed on oxygen sites in $\text{Ni}^{\text{III}}\text{-OOH}$ species are hardly to cleavage (Figure

RESEARCH ARTICLE

6g), likely due to the weaker activation effects of the Ni *d*-orbital on C–C bonds^[25]. Additionally, the Pourbaix diagrams, derived from pH-dependent catalytic activity tests, exhibit that the slope of Ni-BPDA/OKB is consistently around 122 mV pH⁻¹ (Figure 6h and Figure S61). Thus, the high slope demonstrates that the EG oxidation can be significantly influenced by the OH⁻ nucleophilic attack^[26]. Overall, the organic electrooxidation processes on Ni-based molecular complexes are illustrated in Figure 6i. The hypervalent Ni^{III}-OOH species, acting as proton acceptors, facilitate the dehydrogenation of C–H bonds through rapid proton abstraction, which helps regenerate the Ni-organic coordination centers. The direct adsorption of organic substrates on atomically exposed nickel sites would promote C–C bond cleavage via the activation of Ni *d* orbital. Additionally, the OH⁻ nucleophilic attack can also assist in C–C bonds cleavage and formate formation.

Conclusion

A series of molecular complexes were developed by coordinating aromatic organic ligands with nickel on oxygen-functional ketjenblack. This configuration is optimized to modulate the Ni-organic coordination structure for dynamic generation of Ni^{III}-OOH. Typically, the Ni-BPDA/OKB electrocatalyst demonstrated the ability to electrooxidize 18 different substrate molecules. Especially, the methanol and EG oxidation achieved high mass activity of 4.38 and 4.26 A mg_{Ni}⁻¹ at 1.45 V, respectively. *In situ* characterizations and theoretical analysis revealed that the atomically exposed Ni^{III}-OOH sites with unoccupied *d* orbital enable direct adsorption of organic reactants, thus achieving feasible C–H and C–C bonds cleavage. The proton abstraction from C–H bonds to Ni^{III}-OOH can induce the reversible redox transition between Ni^{II}-OH and Ni^{III}-OOH, thereby stabilizing the coordination structures. This study provides essential insights into the mechanisms of organic nucleophile oxidation on innovative molecular complexes sites.

Acknowledgements

This work was financially supported by the National Natural Science Foundation of China (22175108, 22409123 & 22379086), the Natural Science Foundation (ZR2022ZD27, ZR2024QB113) of Shandong Province, Taishan Scholars Program (No. tstp20221105) of Shandong Province, China Postdoctoral Science Foundation (2024M761783), and Postdoctoral Fellowship Program of CPSF (GZC20231443). The authors also acknowledge the assistance of the Analytical Center for Structural Constituent and Physical Property of Core Facilities Sharing Platform (Shandong University), and the 1W1B station in the BSRF for help with XAS characterizations.

Keywords: Electrocatalysis • supported catalysts • coordination design • atomically exposed nickel sites • C–C bond cleavage.

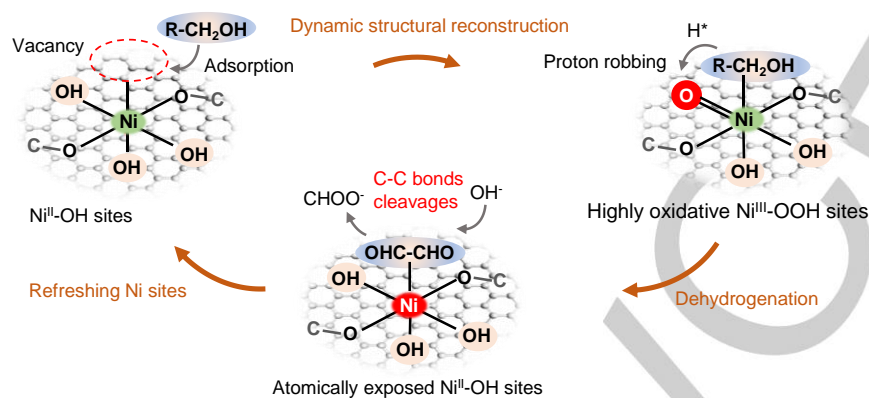
- [1] aC. Liu, F. Chen, B.-H. Zhao, Y. Wu, B. Zhang, *Nat. Rev. Chem.* **2024**, *8*, 277–293; bY. Lu, M. Chen, Y. Wang, C. Yang, Y. Zou, S. Wang, *Chem* **2024**, *10*, 1371–1390; cJ. Chen, F. Zhang, M. Kuang, L. Wang, H. Wang, W. Li, J. Yang, *Proc. Nat. Acad. Sci.* **2024**, *121*, e2318853121.
- [2] G. Fu, X. Kang, Y. Zhang, Y. Guo, Z. Li, J. Liu, L. Wang, J. Zhang, X.-Z. Fu, J.-L. Luo, *Nat. Commun.* **2023**, *14*, 8395.
- [3] R. Wang, Y. Kang, J. Wu, T. Jiang, Y. Wang, L. Gu, Y. Li, X. Yang, Z. Liu, M. Gong, *Angew. Chem. Int. Ed.* **2022**, *61*, e202214977.
- [4] aH. Zhou, Y. Ren, Z. Li, M. Xu, Y. Wang, R. Ge, X. Kong, L. Zheng, H. Duan, *Nat. Commun.* **2021**, *12*, 4679; bY. Yan, H. Zhou, S.-M. Xu, J. Yang, P. Hao, X. Cai, Y. Ren, M. Xu, X. Kong, M. Shao, Z. Li, H. Duan, *J. Am. Chem. Soc.* **2023**, *145*, 6144–6155.
- [5] S.-K. Geng, Y. Zheng, S.-Q. Li, H. Su, X. Zhao, J. Hu, H.-B. Shu, M. Jaroniec, P. Chen, Q.-H. Liu, S.-Z. Qiao, *Nat. Energy* **2021**, *6*, 904–912.
- [6] a) Y. He, Z. Ma, F. Yan, C. Zhu, T. Shen, S. Chou, X. Zhang, Y. Chen, *Proc. Nat. Acad. Sci.* **2024**, *121*, e2320777121; b) Y. Qi, Y. Zhang, L. Yang, Y. Zhao, Y. Zhu, H. Jiang, C. Li, *Nat. Commun.* **2022**, *13*, 4602; c) C. Yang, Z. Wu, Y. Zheng, Y. Gao, T. Ma, Z. Zeng, Y. Wang, C. Cheng, S. Li, *Adv. Funct. Mater.*, **2024**, 2404061; d) C. Yang, Z. Wu, Z. Zhao, Y. Gao, T. Ma, X. Luo, C. Cheng, Y. Wang, S. Li, C. Zhao, *Adv. Mater.* **2023**, *35*, 2303331.
- [7] a) Y. Wang, J. Ma, X. Cao, S. Chen, L. Dai, J. Zhang, *J. Am. Chem. Soc.* **2023**, *145*, 20624–20633; b) Y. Hao, J. Li, X. Cao, L. Meng, J. Wu, X. Yang, Y. Li, Z. Liu, M. Gong, *ACS Catal.* **2023**, *13*, 2916–2927; c) D. Chen, Y. Ding, X. Cao, L. Wang, H. Lee, G. Lin, W. Li, G. Ding, L. Sun, *Angew. Chem. Int. Ed.* **2023**, *62*, e202309478.
- [8] Y. Yan, J. Zhong, R. Wang, S. Yan, Z. Zou, *J. Am. Chem. Soc.* **2024**, *146*, 4814–4821.
- [9] a) S. Li, R. Ma, J. Hu, Z. Li, L. Liu, X. Wang, Y. Lu, G. E. Sterbinsky, S. Liu, L. Zheng, J. Liu, D. Liu, J. Wang, *Nat. Commun.* **2022**, *13*, 2916; b) W. Chen, C. Xie, Y. Wang, Y. Zou, C.-L. Dong, Y.-C. Huang, Z. Xiao, Z. Wei, S. Du, C. Chen, B. Zhou, J. Ma, S. Wang, *Chem* **2020**, *6*, 2974–2993; c) Y. Hao, J. Li, X. Cao, L. Meng, J. Wu, X. Yang, Y. Li, Z. Liu, M. Gong, *ACS Catal.* **2023**, *13*, 2916–2927.
- [10] Y. Li, X. Wei, L. Chen, J. Shi, M. He, *Nat. Commun.* **2019**, *10*, 5335.
- [11] a) W. Chen, J. Shi, C. Xie, W. Zhou, L. Xu, Y. Li, Y. Wu, B. Wu, Y.-C. Huang, B. Zhou, M. Yang, J. Liu, C.-L. Dong, T. Wang, Y. Zou, S. Wang, *Natl. Sci. Rev.* **2023**, *10*; b) X. Wu, Y. Wang, Z.-S. Wu, *Chem* **2022**, *8*, 2594–2629; c) P. Wang, J. Zheng, X. Xu, Y.-Q. Zhang, Q.-F. Shi, Y. Wan, S. Ramakrishna, J. Zhang, L. Zhu, T. Yokoshima, Y. Yamauchi, Y.-Z. Long, *Adv. Mater.* **2024**, *36*, 2404806.
- [12] a) J. Qi, Y. Du, Q. Yang, N. Jiang, J. Li, Y. Ma, Y. Ma, X. Zhao, J. Qiu, *Nat. Commun.* **2023**, *14*, 6263; b) J. He, Y. Tong, Z. Wang, G. Zhou, X. Ren, J. Zhu, N. Zhang, L. Chen, P. Chen, *Proc. Nat. Acad. Sci.* **2024**, *121*, e2405846121.
- [13] a) F. Liu, X. Gao, R. Shi, Z. Guo, E. C. M. Tse, Y. Chen, *Angew. Chem. Int. Ed.* **2023**, *62*, e202300094; b) W. Chen, J. Shi, Y. Wu, Y. Jiang, Y.-C. Huang, W. Zhou, J. Liu, C.-L. Dong, Y. Zou, S. Wang, *Angew. Chem. Int. Ed.* **2024**, *63*, e202316449; c) J. Wu, R. Wang, Y. Kang, J. Li, Y. Hao, Y. Li, Z. Liu, M. Gong, *Angew. Chem. Int. Ed.* **2024**, *63*, e202403466.
- [14] a) R. Buller, S. Lutz, R. J. Kazlauskas, R. Snajdrova, J. C. Moore, U. T. Bornscheuer, *Science* **2023**, *382*, ead8615; b) S. Shi, P. Yang, C. Dun, W. Zheng, J. J. Urban, D. G. Vlachos, *Nat. Commun.* **2023**, *14*, 429.
- [15] a) S. Lyu, C. Guo, J. Wang, Z. Li, B. Yang, L. Lei, L. Wang, J. Xiao, T. Zhang, Y. Hou, *Nat. Commun.* **2022**, *13*, 6171; b) W. Zheng, L. Y. S. Lee, *ACS Energy Lett.* **2021**, *6*, 2838–2843; c) Y. Wang, L. Zhao, J. Ma, J. Zhang, *Energy Environ. Sci.* **2022**, *15*, 3830–3841.
- [16] a) X. Mo, Y. Deng, S. K.-M. Lai, X. Gao, H.-L. Yu, K.-H. Low, Z. Guo, H.-L. Wu, H. Y. Au-Yeung, E. C. M. Tse, *J. Am. Chem. Soc.* **2023**, *145*, 6087–6099; b) J. Ke, M. Chi, J. Zhao, Y. Liu, R. Wang, K. Fan, Y. Zhou, Z. Xi, X. Kong, H. Li, J. Zeng, Z. Geng, *J. Am. Chem. Soc.* **2023**, *145*, 9104–9111; c) M. Liu, N. Li, X. Wang, J. Zhao, D.-C. Zhong, W. Li, X.-H. Bu, *Angew. Chem. Int. Ed.* **2023**, *62*, e202300507.
- [17] J. Kang, X. Qiu, Q. Hu, J. Zhong, X. Gao, R. Huang, C. Wan, L.-M. Liu, X. Duan, L. Guo, *Nat. Catal.* **2021**, *4*, 1050–1058.
- [18] a) Z. Chen, J. Li, L. Meng, J. Li, Y. Hao, T. Jiang, X. Yang, Y. Li, Z.-P. Liu, M. Gong, *Nat. Commun.* **2023**, *14*, 1184; b) J. Kang, X. Qiu, Q. Hu, J. Zhong, X. Gao, R. Huang, C. Wan, L.-M. Liu, X. Duan, L. Guo, *Nat. Catal.* **2021**, *4*, 1050–1058.
- [19] A. J. Neel, M. J. Hilton, M. S. Sigman, F. D. Toste, *Nature* **2017**, *543*, 637–646.
- [20] a) B.-H. Lee, H. Shin, A. S. Rasouli, H. Choubisa, P. Ou, R. Dorakhan, I. Grigioni, G. Lee, E. Shirzadi, R. K. Miao, J. Wicks, S. Park, H. S. Lee, J. Zhang, Y. Chen, Z. Chen, D. Sinton, T. Hyeon, Y.-E. Sung, E. H. Sargent, *Nat. Catal.* **2023**, *6*, 234–243; b) S. Yuan, J. Peng, B. Cai, Z. Huang, A. T. Garcia-Esparza, D. Sokaras, Y. Zhang, L. Giordano, K. Akkiraju, Y. G. Zhu, R. Hübner, X. Zou, Y. Román-Leshkov, Y. Shao-Horn, *Nat. Mater.* **2022**, *21*, 673–680; c) J. Su, C. B. Musgrave, Y. Song, L. Huang, Y. Liu, G. Li, Y. Xin, P. Xiong, M. M.-J. Li, H. Wu, M. Zhu, H. M. Chen, J. Zhang, H. Shen, B. Z. Tang, M. Robert, W. A. Goddard, R. Ye, *Nat. Catal.* **2023**, *6*, 818–828.
- [21] S. Li, B. Chen, Y. Wang, M.-Y. Ye, P. A. van Aken, C. Cheng, A. Thomas, *Nat. Mater.* **2021**, *20*, 1240–1247.
- [22] Y. Luo, L. Tang, U. Khan, Q. Yu, H.-M. Cheng, X. Zou, B. Liu, *Nat. Commun.* **2019**, *10*, 269.
- [23] X. Liu, Y.-Q. Zhu, J. Li, Y. Wang, Q. Shi, A.-Z. Li, K. Ji, X. Wang, X. Zhao, J. Zheng, H. Duan, *Nat. Commun.* **2024**, *15*, 7685.
- [24] Q. Qian, X. He, Z. Li, Y. Chen, Y. Feng, M. Cheng, H. Zhang, W. Wang, C. Xiao, G. Zhang, Y. Xie, *Adv. Mater.* **2023**, *35*, 2300935.
- [25] a) Y. Yan, R. Wang, Q. Zheng, J. Zhong, W. Hao, S. Yan, Z. Zou, *Nat. Commun.* **2023**, *14*, 7987; b) S. Shen, H. Zhang, K. Song, Z. Wang, T. Shang, A. Gao, Q. Zhang, L. Gu, W. Zhong, *Angew. Chem. Int. Ed.* **2024**, *63*, e202315340.

RESEARCH ARTICLE

- [26] H. Yang, F. Li, S. Zhan, Y. Liu, W. Li, Q. Meng, A. Kravchenko, T. Liu, Y. Yang, Y. Fang, L. Wang, J. Guan, I. Furó, M. S. G. Ahlquist, L. Sun, *Nat. Catal.* **2022**, 5, 414-429.

RESEARCH ARTICLE

Entry for the Table of Contents



Molecular electrocatalysts featuring atomically dispersed nickel sites were synthesized via coordination with aromatic ligands on functionalized carbon black, enabling efficient electrooxidation of diverse organic substrates with high peak current densities. The dynamic transition of nickel centers facilitates C–H and C–C bond cleavage, driving the overall catalytic performance.